PAPER

Bimetallic phosphide decorated Mo–BiVO₄ for significantly improved photoelectrochemical activity and stability†

Jie Qi,‡[ab] Dechao Kong,‡[ab] Danyang Liu,[c] Lun Pan, [ID] *[ab] Ying Chen,[ab] Xiangwen Zhang[ab] and Ji-Jun Zou [ID] *[ab]

Bismuth vanadate photoanode has shown great potential for photoelectrochemical (PEC) catalysis, but it needs to be further modified because of its relatively low charge-separation efficiency and poor stability. Herein, the bimetallic phosphide NiCoP decorated Mo–BiVO₄ is fabricated through the electrodeposition and drop-casting method, which significantly improves the charge separation and surface oxidation reaction. Therefore, the fabricated NiCoP/Mo–BiVO₄ photoanode exhibits a low onset potential of 0.21 V (*vs.* RHE) and high photocurrent of 3.21 mA cm^{-2} at 1.23 V (*vs.* RHE), which is 3.12 times higher than that of pure BiVO₄. Importantly, the decoration of NiCoP significantly improve the stability of BiVO₄ photoanode.

1. Introduction

Photoelectrochemical (PEC) water splitting is considered as one of the most promising strategies to convert solar energy to hydrogen energy, and meet the increasing demand for clean and renewable fuel technologies.[1,2] In the past few decades, great efforts have been made to improve the activity of photoanodes.[3] Up to now, various photoanodes have been developed, such as TiO₂, ZnO, Fe₂O₃, WO₃, BiVO₄, *etc.*[4–8] In particular, BiVO₄ has shown great potential for water oxidation due to its narrow band gap for visible-light absorption, appropriate valence band (VB) position for water oxidation, plentiful abundance, low cost and so on.[9] However, limited by rapid recombination of photogenerated charges and relatively slow oxidation kinetics, the practical activity of BiVO₄ for PEC water splitting is much lower than its theoretical photocurrent density of 7.6 mA cm^{-2} (under solar light illumination).[10]

Doping transition metal ions have been proved to be an effective way to overcome the limitation of charge separation and migration.[11,12] Especially, among various metal ions, Mo is reported to be the better one to enhance the PEC activity of

BiVO₄.[13] Moreover, in order to accelerate the surface reaction kinetics, decorating adequate oxygen evolution cocatalysts on semiconductors is well accepted, which can effectively lower the activation energy of water oxidation reaction and further decrease the rate of charge recombination.[14,15] Actually, many electrocatalysts have been loaded on photoanodes as cocatalysts, such as FeOOH/NiOOH, Co₃O₄ and Co-Pi.[8,16–18] Recently, transition metal phosphides have been paid great attention to be used as promising cocatalysts, for their good performance for oxygen evolution reaction (OER) in electrochemical water splitting.[19] It is worth noting that the bimetallic phosphide presents higher activity for OER than the corresponding monometal phosphides due to the presence of the synergistic effect.[20,21] However, there are few researches about the decoration of bimetallic phosphides on doped BiVO₄ for PEC catalysis.

In this work, we combined the effect of Mo doping and decoration of bimetallic phosphide cocatalyst to fabricate NiCoP/Mo–BiVO₄ photoanode for PEC water oxidation. With 1.57% Mo doping and 2% NiCoP decoration, NiCoP/Mo–BiVO₄ photoanode demonstrates very high PEC performance, with the low onset potential of 0.21 V *vs.* RHE, and the photocurrent density of 3.21 mA cm^{-2} at 1.23 V *vs.* RHE. It is worth noting that the decoration of NiCoP on Mo–BiVO₄ photoanode significantly improves the PEC stability.

[a]Key Laboratory for Green Chemical Technology of the Ministry of Education, School of Chemical Engineering and Technology, Tianjin University, Tianjin 300072, China. E-mail: panlun76@tju.edu.cn; jj_zou@tju.edu.cn

[b]Collaborative Innovative Center of Chemical Science and Engineering (Tianjin), Tianjin 300072, China

[c]People's Public Security University of China, Beijing 100038, China

† Electronic supplementary information (ESI) available. See DOI: 10.1039/c9ra02105a

‡ The authors contributed to this work equally.

2. Experimental

2.1 Materials

Bi(NO₃)₃·H₂O, Ni(NO₃)₂·6H₂O, KI, *p*-benzoquinone, KOH, Na₂SO₄, NaH₂PO₂, and absolute ethanol were all obtained from Aladdin Chemicals. VO(acac)₂, NiCl₂ and CoCl₂ were

gained from J&K Scientific Ltd. Dimethyl sulfoxide (DMSO), HCl and HNO_3 were purchased from Tianjin GuangFu Fine Chemical Research Institute. Deionized water (>18 MΩ cm) supplied by a UP Water Purification System was used in all experiments. Fluorine doped tin oxide substrates (FTO, 1.1 mm thick, 14 Ω per square) were purchased from WuHan Jinge-solar Energy Technology Co., Ltd. Before using, the FTO substrates were cleaned under sonication in acetone, ethanol, and deionized water.

2.2 Sample preparation

2.2.1 BiVO₄ photoanodes. As the precursor of $BiVO_4$, BiOI was prepared through electrodeposition. Briefly, 0.97 g $Bi(NO_3)_3 \cdot H_2O$ was dissolved in 50 mL of a 0.4 M KI solution with pH of 1.7. After stirring for 30 min, the above solution was mixed with 20 mL absolute ethanol containing 0.497 g p-benzoquinone. Then, the electro-deposition of BiOI films was performed potentiostatically at −0.1 V vs. Ag/AgCl at room temperature for 180 s in the typical three-electrode system, with an FTO substrate (2.5 × 2 cm²) as working electrode, a Pt wire as counter electrode and the saturated Ag/AgCl as reference electrode. Subsequently, 200 μL dimethyl sulfoxide (DMSO) solution containing 0.2 M vanadyl acetylacetonate (VO(acac)₂) dripped on the obtained BiOI electrodes and then annealed in a muffle furnace at 450 °C for 2 h with a heating rate of 2 °C min⁻¹. Afterwards, the electrodes were soaked in 1 M NaOH solution to remove the excess V_2O_5 on the surface of $BiVO_4$ films. Then, the obtained $BiVO_4$ photoanodes were rinsed with deionized water and dried in ambient air.

2.2.2 Mo-doped BiVO₄ photoanodes. 2 mM $(NH_4)_2MoO_4$ solution was used as Mo source and dropped on $BiVO_4$ electrodes with a certain volume by a pipette, followed by heating in a muffle furnace at 450 °C (ramping rate 2 °C min⁻¹) for 2 h. After annealing, the as-prepared electrodes were immersed in 1 M NaOH solution to remove the excess MoO_3. Then, the obtained Mo-doped $BiVO_4$ photoanodes (denoted as Mo–$BiVO_4$) were washed by deionized water and dried. The Mo doped amount is about 1.57% (tested by ICP detection), similar to the literature.[18]

2.2.3 NiCoP/Mo–BiVO₄ photoanodes. NiCoP nanoparticles were obtained via a simple solid-state reaction by reacting the NiCo(OH)₂ precursors with NaH_2PO_2. Briefly, 250 mg sodium citrate and 2 g of NaOH were dissolved in 80 mL deionized water under sonication for 30 min to generate a homogeneous solution. Then, 20 mL mixed solution containing 1.204 mmol $NiCl_2$ and 2.236 mmol $CoCl_2$ was slowly injected into the above aqueous solution. After stirring for 1 h, the product was collected by centrifugation and washed with deionized water and ethanol. Then the obtained NiCo(OH)₂ precursors were dried under vacuum. In order to obtain NiCoP nanoparticles, 200 mg NiCo(OH)₂ and 1 g NaH_2PO_2 were mechanically blended and grinded into a fine powder and then heated at 300 °C in a quartz tube for 2 h under an Ar flow. After cooling to room temperature, the obtained products were thoroughly disposed with 1 M HCl, and washed subsequently with deionized water

and ethanol. Then the obtained NiCoP nanoparticles were dried under vacuum at 60 °C for 10 hours.

A drop-casting technique was used to prepare the NiCoP/Mo–$BiVO_4$ photoanode. Firstly, 20 mg of NiCoP nanoparticles were dispersed in 10 mL absolute ethanol and ultrasonicated for 2 h to form a uniform suspension, and 30 μL above suspension was drop-casted onto the Mo–$BiVO_4$ samples to prepare NiCoP/Mo–$BiVO_4$ photoanodes.

For NiCoP/Mo–$BiVO_4$, the Mo doped amount is ca. 1.57%, and the NiCoP deposition amount is chosen as ca. 2%, because it shows the highest PEC performance in water splitting (Fig. S1, ESI†).

2.2.4 NiP/Mo–BiVO₄ and CoP/Mo–BiVO₄ photoanodes. 30 μL of 2 mg mL⁻¹ uniform NiP or CoP suspensions were drop-casted onto Mo-doped $BiVO_4$ electrodes to prepare NiP/Mo–$BiVO_4$ and CoP/Mo–$BiVO_4$, respectively.

2.3 Characterization

The crystalline phases were characterized by X-ray diffractometer (D/MAX-2500) with Cu Kα radiation (λ = 1.5416 Å) at 40 kV and 140 mA at a scanning rate of 5° min⁻¹. X-ray photoelectron spectrum (XPS) was conducted with a PHI-1600 X-ray photoelectron spectroscope equipped with Al K radiation. The morphology and microstructure of the samples were observed by field-emission scanning electron microscopy (SEM) (Hitachi S-4800). And transmission electron microscopy (TEM) and high-resolution TEM (HRTEM) images were obtained using a JEOL JEM-2100F microscope at 200 kV. The energy dispersive spectrometer (EDS-mapping) characterization was carried out with an EDX system attached to TEM. Raman spectra were recorded with a Raman spectrometer (DXR Microscope), and a green semiconductor laser (532 nm) was used as the excitation source. The optical properties of the products were analyzed with UV-vis diffuse reflectance spectra (UV-vis DRS) obtained from a Hitachi U-3010 spectrometer equipped with a 60 mm diameter integrating sphere using $BaSO_4$ as reflectance sample. The amount of NiCoP was measured by Inductively coupled plasma (ICAP6300 Duo).

2.4 Photoelectrochemical (PEC) measurements

PEC performances of the photoanodes were evaluated by CHI 660E electrochemical workstation using a typical three-electrode electrochemical cell with the as-prepared electrodes as working electrode, a Pt wire as counter electrode, and saturated Ag/AgCl as reference electrode. The illumination source was a 300 W xenon arc lamp (100 mW cm⁻², PLS-SXE300UV, Beijing Trusttech. Co. Ltd) equipped with an AM 1.5G filter. The tests were performed in the electrolyte of 0.5 M Na_2SO_4 solution (pH = 6.8) with or without 1 M Na_2SO_3 as a hole scavenger. The scan rate of the linear sweep voltammetry (LSV) test was 10 mV s⁻¹. All measurements were carried out with Ag/AgCl reference electrode, and the potential vs. Ag/AgCl reference electrode was converted to the potential vs. RHE according to the equation:

$$E \ (vs. \ \text{RHE}) = E \ (vs. \ \text{Ag/AgCl}) + 0.059\text{pH} + 0.197 \quad (1)$$

The incident-photo-to-current efficiency (IPCE) tests were performed at a bias of 1.23 V *vs.* RHE as the wavelength from 350 nm to 600 nm. And the IPCE was calculated according to the following equation:

$$IPCE(\lambda) = \frac{1240 \times J(\lambda)}{\lambda \times P(\lambda)} \qquad (2)$$

where λ is the wavelength (nm), $J(\lambda)$ is the photocurrent density (mA cm^{-2}), and $P(\lambda)$ is the incident power density of the monochromatic light (mW cm^{-2}).

The applied-bias power efficiency (ABPE) for PEC water splitting was evaluated using the following equation:

$$ABPE = \frac{I \times (1.23 - V_{app})}{P_{light}} \times 100\% \qquad (3)$$

where V_{app} is the applied voltage *vs.* RHE, I is the measured current density, and P_{light} is the power density of the illumination.

Electrochemical impedance spectra (EIS) measurements were carried out with a sinusoidal ac perturbation of 10 mV applied over the frequency range of 1–10^5 Hz.

2.5 Photoelectrochemical H$_2$ and O$_2$ evolution measurements

Using Ar as a carrier gas, H$_2$ and O$_2$ gases evolved from the PEC cell were analyzed using a gas chromatograph (450-GC, molecular sieve 5 L column) equipped with a thermal conductivity detector (TCD). The light source and electrolyte were the same as those used for the above PEC measurements, and the gas products were sampled at each 20 min.

3. Result and discussion

3.1 Crystal structure

As shown in Fig. 1a (XRD patterns), BiVO$_4$, Mo–BiVO$_4$ (with 1.57% Mo doping) and NiCoP/Mo–BiVO$_4$ (with 1.57% Mo doping and 2% NiCoP decoration) photoanodes all possess the typical diffraction peaks of monoclinic scheelite BiVO$_4$ (JCPDS no. 14-0688)[22] with high crystallinity, while the characteristic peaks of SnO$_2$ (JCPDS no. 41-1445) are attributed to the FTO glass.[8] No diffraction peaks of Mo species are detected for Mo–BiVO$_4$, suggesting the absence of other Mo impurities.[13] Meanwhile, there are no diffraction peaks of NiCoP observed for

NiCoP/Mo–BiVO$_4$, which should be owing to the small particle size and uniform dispersion of NiCoP on the surface of Mo–BiVO$_4$.

To further verify the crystal structure, the Raman spectra (Fig. 1b) was also measured. BiVO$_4$ exhibits five main Raman peaks, respectively located at *ca.* 133, 216, 332, 374 and 834 cm^{-1}, attributed to the active Raman scattering modes of monoclinic scheelite BiVO$_4$.[23,24] The peaks at 133 and 216 cm^{-1} correspond to the external modes of BiVO$_4$, while the peaks at 332 and 374 cm^{-1} are attributed to the asymmetric and symmetric deformation modes of the VO$_4$$^{3-}$ tetrahedron (δ_{as} (VO^{3-}) and δ_s (VO^{3-})), respectively.[24] The peak at 834 cm^{-1} is related to the V–O stretching mode of pure BiVO$_4$, and it shifts to lower frequencies (831 cm^{-1}) for Mo–BiVO$_4$ and NiCoP/Mo–BiVO$_4$, which should be caused by the longer bond lengths of Mo–O bond (Mo^{6+}, 0.41 Å) than V–O bond (V^{5+}, 0.36 Å), proving Mo has been successfully doped into BiVO$_4$.[25]

As shown in Fig. 2a, BiVO$_4$ displays a porous crystal structure, with a film thickness of *ca.* 0.98 μm and the size of BiVO$_4$ nanoparticles of 200–400 nm. From Fig. 2b, Mo doping has no influence on the morphology of BiVO$_4$ and no Mo-related impurities can be observed, suggesting the effective Mo doping. However, the deposition of NiCoP on Mo–BiVO$_4$ leads to a rough surface with many interconnected nanoparticles (NPs) decorated (Fig. 2c). According to TEM image (Fig. 2d and e), the NiCoP NPs, with the crystal size of 5–10 nm, uniformly disperse on Mo–BiVO$_4$ surface. The lattice spacing distances of 0.26 nm and 0.230 nm are corresponding to the interplanar spacing of BiVO$_4$ (020) plane and NiCoP (111) plane, respectively. The STEM elemental mapping images show that the elements of Bi, V, Mo, Ni, Co and P are uniformly dispersed in NiCoP/Mo–BiVO$_4$ (Fig. 2f–k). All the above results suggest that Mo element has been doped in BiVO$_4$ and the NiCoP NPs are uniformly decorated on Mo–BiVO$_4$ surface.

3.2 Chemical states and optical absorption

The chemical composition and surface elemental states of as-prepared photoanodes were tested by X-ray photoelectron
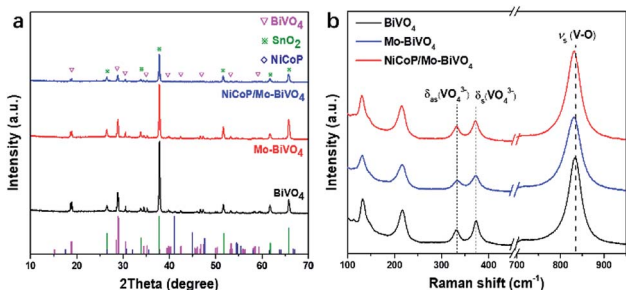

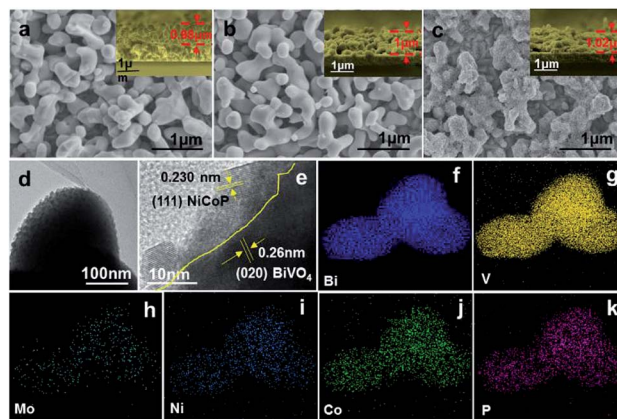Fig. 1 XRD patterns (a) and Raman spectra (b) of BiVO$_4$, Mo–BiVO$_4$ and NiCoP/Mo–BiVO$_4$.

Fig. 2 Top-view and cross-sectional-view (the inset figure) SEM images of pure BiVO$_4$ (a), Mo–BiVO$_4$ (b) and NiCoP/Mo–BiVO$_4$ (c). TEM and STEM elemental mapping images of NiCoP/Mo–BiVO$_4$ (d–k).

spectroscopy (XPS). In Fig. 3a, pure $BiVO_4$ shows binding energies of $Bi4f_{5/2}$ and $Bi4f_{7/2}$ at *ca.* 164 eV and 159 eV, respectively, which are the characteristic peaks of Bi^{3+} species.[12,18] The signals of V2p (Fig. 3b) are located at *ca.* 524 eV and 516.6 eV, corresponding to $V2p_{1/2}$ and $V2p_{3/2}$ respectively, referring to V^{5+} species.[26] For Mo–$BiVO_4$ and NiCoP/Mo–$BiVO_4$, the peaks for Bi4f and V2p shift to higher binding energy compared to pure $BiVO_4$, owing to the higher electronegativities of Mo^{6+} than V^{5+}.[13,27] Furthermore, Mo can be detected both in Mo–$BiVO_4$ and NiCoP/Mo–$BiVO_4$ samples (Fig. 3c), with two characteristic peaks located at *ca.* 232.1 eV and 235.4 eV, confirming the presence of Mo^{6+} species (substituting V atoms) in $BiVO_4$.[25]

Then, UV-visible diffuse reflectance spectra (DRS) were used to characterize the optical properties of the samples. In Fig. 3d, the absorption edge of $BiVO_4$ appears at *ca.* 525 nm, consistent with its intrinsic band gap of 2.56 eV.[8,28] After Mo doping in $BiVO_4$, the absorption intensity of Mo–$BiVO_4$ is slightly enhanced in visible-light region, and the band gap is slightly reduced to 2.54 eV.[27] Moreover, NiCoP/Mo–$BiVO_4$ shows an obvious increase in optical absorption intensity in the range below 525 nm, owing to the rough surface.[29] Therefore, the Mo doping and NiCoP decoration strengthen the optical absorption of $BiOV_4$ photoanode.

3.3 PEC performances

To identify the performances of $BiVO_4$, Mo-doped $BiVO_4$ and NiCoP/Mo–$BiVO_4$ photoanodes, PEC water splitting was performed under simulated sun light illumination (100 mW cm^{-2}). As shown in Fig. 4a, pure $BiVO_4$ exhibits a photocurrent of 1.03 mA cm^{-2} at 1.23 V *vs.* RHE and an onset potential of 0.62 V *vs.* RHE. Upon Mo doping (1.57% Mo), Mo–$BiVO_4$ has a higher photocurrent of 2.14 mA cm^{-2} (1.23 V *vs.* RHE) and a lower onset potential of 0.49 V (*vs.* RHE). Furthermore, after the decoration of NiCoP with the optimal amount of *ca.* 2% (Fig. S1, ESI†), NiCoP/Mo–$BiVO_4$ shows the highest photocurrent density
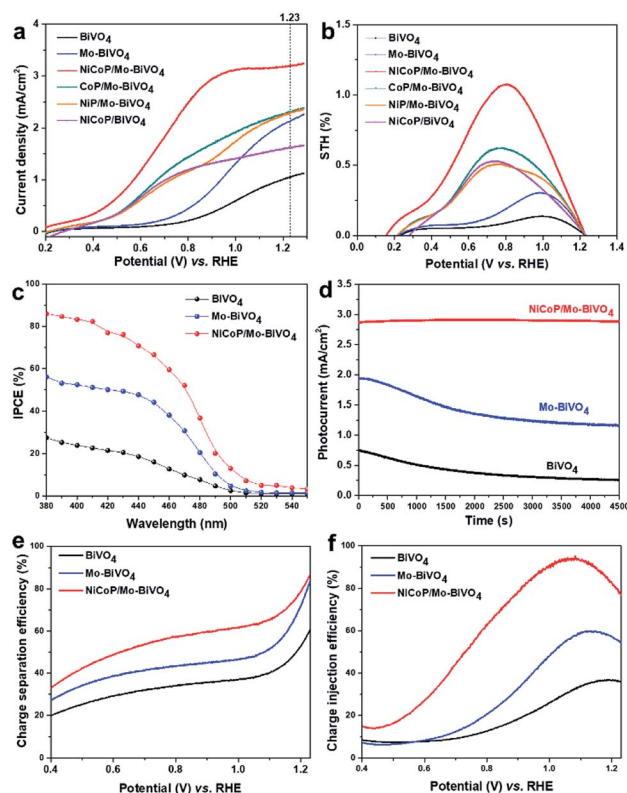

Fig. 4 *J–V* curves under AM 1.5G illumination (a), ABPE (b), IPCE spectra measured at 1.23 V *vs.* RHE (c), amperometric *I–t* curves plotted at 1.1 V *vs.* RHE (d), charge separation efficiency (e) and charge injection efficiency (f) of as-prepared samples.

of 3.21 mA cm^{-2} at 1.23 V *vs.* RHE (almost 3.12 times higher than $BiVO_4$) and lowest onset potential of 0.21 V *vs.* RHE. It is worth noting that, the NiCoP decoration exhibits much higher co-catalytic activity than the monometal phosphides (*ca.* 2%), CoP and NiP.

Then, the applied bias photon-to-current conversion efficiency (ABPE) is calculated from the corresponding linear sweep voltammetry curve. Obviously, NiCoP/Mo–$BiVO_4$ shows the highest ABPE of 1.08% at 0.80 V *vs.* RHE (Fig. 4b), which is about 8.31 times than $BiVO_4$ photoanode (0.13% at 1.03 V) and 3.48 times higher than Mo–$BiVO_4$ photoanode (0.31% at 0.99 V), corresponding to their PEC performances. Further for incident photon-to-electron conversion efficiency (IPCE, Fig. 4c), $BiVO_4$ shows low IPCE of *ca.* 22% in the range of 380–450 nm, owing to the fast charge recombination, while the IPCEs of Mo–$BiVO_4$ and NiCoP/Mo–$BiVO_4$ are improved to 54% and >78%, respectively. The above results indicate the Mo doping and NiCoP deposition perform very high ability to significantly improve the PEC activity of $BiVO_4$.

Furthermore, the PEC stabilities of the samples are tested at 1.1 V *vs.* RHE. As shown in Fig. 4d, $BiVO_4$ shows very poor stability, with its photocurrent only maintaining 34.7% of the initial value after tested for 4500 s, which is caused by the dissolution of V^{5+} in electrolyte.[9] As shown in Table S1 (ESI†), after Mo doping in $BiVO_4$, the dissolved amounts of Bi and V in the used electrolyte after stability testing are slightly decreased
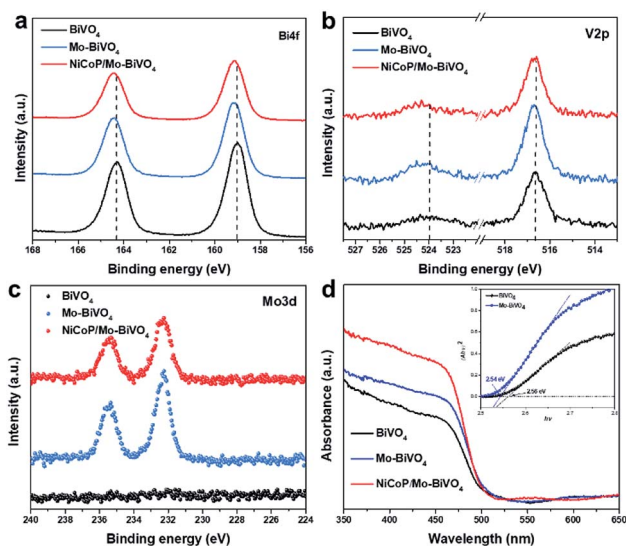

Fig. 3 XPS spectra of Bi4f (a), V2p (b), Mo3d (c) and UV-vis DRS (d) for $BiVO_4$, Mo–$BiVO_4$ and NiCoP/Mo–$BiVO_4$.

compared with pure $BiVO_4$, however, its stability is still poor. Specially, the decoration of NiCoP on Mo–$BiVO_4$ greatly prevents the dissolution of V^{5+} in electrolyte and promotes the PEC stability, without obvious decrease of photocurrent for 4500 s, which should be attributed to its ability to rapidly capture and consume the photogenerated holes. In addition, after stability test (over 4500 s), NiCoP/Mo–$BiVO_4$ shows the same X-ray diffraction peaks (XRD patterns in Fig. S3a, ESI†) and almost similar surface morphology of a rough porous crystal structure with many interconnected nanoparticles (SEM images in Fig. S3b, ESI†) with the samples before stability test, also confirming the high photostability of NiCoP/Mo–$BiVO_4$ film.

In addition, to identify the effects of Mo doping and NiCoP decoration on the charge separation and transfer of $BiVO_4$, the charge separation efficiency (η_{sep}) and charge injection efficiency (η_{inj}), are calculated by J–V curves measured without and with 0.1 M Na_2SO_3 as the hole scavenger in electrolyte.[30] From the J–V curves for sulfite oxidation under light illumination (Fig. 4e, ESI†), the η_{sep} of $BiVO_4$ is 59.5% at 1.23 V $vs.$ RHE, which is much lower than those of Mo–$BiVO_4$ (83.5% at 1.23 V $vs.$ RHE) and NiCoP/Mo–$BiVO_4$ (86%) photoanodes, clearly indicating the improvement of η_{sep} is mainly caused by Mo doping. The doped Mo enhances the charge separation and transfer, and further accelerates the photogenerated holes rapidly transferring to the interface of photoanodes/electrolyte.[18,27] Moreover, the η_{inj} represents the yield of holes that are injected into the electrolyte to oxidize the water.[31] As shown in Fig. 4f (Fig. S2, ESI†), the η_{inj} values of $BiVO_4$ and Mo–$BiVO_4$ are 36% and 55% at 1.23 V $vs.$ RHE, respectively, while that of NiCoP/Mo–$BiVO_4$ reaches as high as 78%, confirming that NiCoP can greatly enhance the surface charge oxidation kinetics to facilitate the process of surface water oxidation.

To further investigate the charge transportation and PEC water oxidation kinetics of the synthesized photoanodes, the electrochemical impedance spectroscopy (EIS) was measured at 0.9 V $vs.$ RHE under light illumination (Fig. 5a). The arc radius of Nyquist plots reflects the charge-transfer behavior at the photoanode/electrolyte interface, and a smaller arc radius implies a lower charge-transfer resistance.[32] Obviously, the arc radius of NiCoP/Mo–$BiVO_4$ is the smallest among all photoanodes, suggesting the Mo doping and NiCoP decoration can lower the charge-transfer resistance and promote the charge

transportation of $BiVO_4$ photoanode. Actually, the main function of NiCoP decoration is the improvement of the PEC water oxidation kinetics of $BiVO_4$, which further accelerate the hole-transfer process.[14]

As shown in Mott–Schottky plots (Fig. 5b), all photoanodes are n-type semiconductors with the positive slope. But the Mo doping and NiCoP decoration cause the gradually slope decrease from $BiVO_4$ to Mo–$BiVO_4$, and NiCoP/Mo–$BiVO_4$, indicating the increased density of charge carriers.[33] When Mo^{6+} substitutes for V^{5+}, it acts as an electron donor in the $BiVO_4$ lattice. Besides, NiCoP, as an effective cocatalyst in PEC water splitting, can capture the photogenerated holes and change the distribution of semiconductor's charge carriers. The holes will transfer from the semiconductor surface to NiCoP nanoparticles, participating in the water oxidation reaction rather than accumulating on the surface of the semiconductors, which will accelerate the holes transfer rate and effectively suppress the recombination of photogenerated electrons and holes. In this way, the doping of Mo and the decoration of NiCoP can all increase the electron density of the photoanodes.

It is noteworthy that the more negative flatband potential leads to the easier generation of photoactive electron, making the whole PEC cell more efficient.[34] From Fig. 5b, NiCoP/Mo–$BiVO_4$ presents more negative flatband potential than Mo–$BiVO_4$ and $BiVO_4$, consistent with the trend of PEC performance. All the above results reveal that the synergistic influence of Mo doping and NiCoP decoration plays an important role to promote the PEC activity and stability of $BiVO_4$ photoanode by increasing the charge carrier density and the surface oxidation kinetics.

3.4 Photoelectrochemical H_2 and O_2 evolution

As shown in Fig. 6, the practical volumes of H_2 and O_2 evolution are close to their theoretical value (at 1.1 V $vs.$ RHE), and the practical volume of hydrogen is nearly twice of oxygen. Meanwhile, the faradaic efficiency of NiCoP/Mo–$BiVO_4$ photoanode is calculated to be more than 95.4%, which can give the evidence that the photocurrent of NiCoP/Mo–$BiVO_4$ photoanode is mainly caused by the water oxidation, excluding the contribution of the NiCoP oxidation.
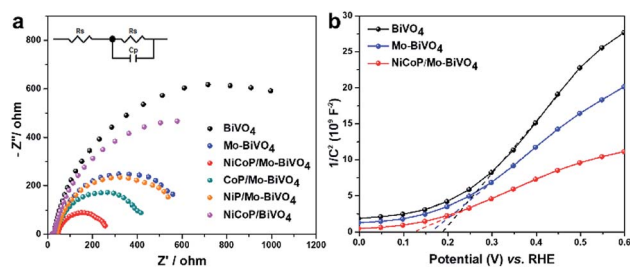

Fig. 5 EIS of as-prepared samples (measured at 0.9 V $vs.$ RHE under illumination) (a), the Mott–Schottky plots measured with a frequency of 100 Hz and amplitude of 10 mV (b).
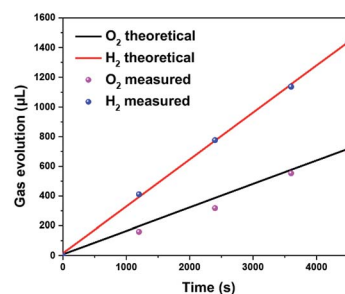

Fig. 6 Gas evolution from the PEC water splitting under light irradiation at an applied bias of 1.1 V $vs.$ RHE in 0.5 M Na_2SO_4 solution (pH = 6.8).

4. Conclusions

In this work, the decoration of bimetallic phosphide NiCoP and Mo doping are adopted to realize the high activity and stability of BiVO$_4$ for PEC water oxidation. With 1.57% Mo doping and 2% NiCoP decoration, NiCoP/Mo–BiVO$_4$ photoanode demonstrates high PEC performance, with the low onset potential of 0.21 V *vs.* RHE, and the photocurrent density of 3.21 mA cm^{-2} at 1.23 V *vs.* RHE. Importantly, NiCoP/Mo–BiVO$_4$ photoanode also exhibits excellent PEC stability, without crystal photocorrosion and PEC current decrease after tested at 1.1 V *vs.* RHE for 4500 s, owing to the rapid consumption of the photogenerated holes *via* NiCoP sites. This work provides the facile approach to fabricate highly active and stable photoanodes by doping and cocatalyst decoration for PEC water splitting.

Conflicts of interest

There are no conflicts of interest to declare.

Acknowledgements

Notes and references

1 L. Pan, S. Wang, J. Xie, L. Wang, X. Zhang and J.-J. Zou, *Nano Energy*, 2016, **28**, 296–303.

2 S. Martha, P. C. Sahooa and K. M. Parida, *RSC Adv.*, 2015, **5**, 61535–61553.

3 Z. Li, W. Luo, M. Zhang, J. Feng and Z. Zou, *Energy Environ. Sci.*, 2013, **6**, 347–370.

4 A. Fujishima and K. Honda, *Nature*, 1972, **238**, 37–38.

5 X. Zhang, Y. Liu and Z. Kang, *ACS Appl. Mater. Interfaces*, 2014, **6**, 4480–4489.

6 P. Zhang, T. Wang, X. Chang and J. Gong, *Acc. Chem. Res.*, 2016, **49**, 911–921.

7 Y. Cui, L. Pan, Y. Chen, N. Afzal, S. Ullah, D. Liu, L. Wang, X. Zhang and J.-J. Zou, *RSC Adv.*, 2019, **9**, 5492–5500.

8 T. W. Kim and K. S. Choi, *Science*, 2014, **343**, 990–994.

9 S. S. M. Bhat and H. W. Jang, *ChemSusChem*, 2017, **10**, 3001–3018.

10 C. Liu, J. Su, J. Zhou and L. Guo, *ACS Sustainable Chem. Eng.*, 2016, **4**, 4492–4497.

11 B. Zhang, H. Zhang, Z. Wang, X. Zhang, X. Qin, Y. Dai, Y. Liu, P. Wang, Y. Li and B. Huang, *Appl. Catal., B*, 2017, **211**, 258–265.

12 L. Yang, Y. Xiong, W. Guo, J. Guo, D. Gao, Y. Zhang and P. Xiao, *Electrochim. Acta*, 2017, **256**, 268–277.

13 K. P. Parmar, H. J. Kang, A. Bist, P. Dua, J. S. Jang and J. S. Lee, *ChemSusChem*, 2012, **5**, 1926–1934.

14 X.-T. Xu, L. Pan, X. Zhang, L. Wang and J.-J. Zou, *Adv. Sci.*, 2018, 1801505.

15 C. Ding, J. Shi, Z. Wang and C. Li, *ACS Catal.*, 2016, **7**, 675–688.

16 D. K. Lee and K.-S. Choi, *Nat. Energy*, 2017, **3**, 53–60.

17 P. Zhang, T. Wang, X.-X. Chang, L. Zhang and J.-L. Gong, *Angew. Chem., Int. Ed.*, 2016, **55**, 5851–5855.

18 S. K. Pilli, T. E. Furtak, L. D. Brown, T. G. Deutsch, J. A. Turner and A. M. Herring, *Energy Environ. Sci.*, 2011, **4**, 5028–5034.

19 F. Yu, H. Zhou, Y. Huang, J. Sun, F. Qin, J. Bao, W. A. Goddard, S. Chen and Z. Ren, *Nat. Commun.*, 2018, **9**, 2551.

20 H. Liang, A. N. Gandi, D. H. Anjum, X. Wang, U. Schwingenschlogl and H. N. Alshareef, *Nano Lett.*, 2016, **16**, 7718–7725.

21 Y. Li, H. Zhang, M. Jiang, Y. Kuang, X. Sun and X. Duan, *Nano Res.*, 2016, **9**, 2251–2259.

22 J.-M. Wu, Y. Chen, L. Pan, P. Wang, Y. Cui, D. Kong, L. Wang, X. Zhang and J.-J. Zou, *Appl. Catal., B*, 2018, **221**, 187–195.

23 J. Yu and A. Kudo, *Adv. Funct. Mater.*, 2006, **16**, 2163–2169.

24 H. Yoon, M. G. Mali, J. Y. Choi, M. W. Kim, S. K. Choi, H. Park, S. S. Al-Deyab, M. T. Swihart, A. L. Yarin and S. S. Yoon, *Langmuir*, 2015, **31**, 3727–3737.

25 H. Jung, S. Y. Chae, H. Kim, B. K. Min and Y. J. Hwang, *Catal. Commun.*, 2016, **75**, 18–22.

26 L. Zhang, D. Chen and X. Jiao, *J. Phys. Chem. B*, 2006, **110**, 2668–2673.

27 Y. Shi, Y. Yu, Y. Yu, Y. Huang, B. Zhao and B. Zhang, *ACS Energy Lett.*, 2018, **3**, 1648–1654.

28 Z. F. Huang, L. Pan, J. J. Zou, X. Zhang and L. Wang, *Nanoscale*, 2014, **6**, 14044–14063.

29 L. Bi, X. Gao, L. Zhang, D. Wang, X. Zou and T. Xie, *ChemSusChem*, 2018, **11**, 276–284.

30 F. Yu, F. Li, T. Yao, J. Du, Y. Liang, Y. Wang, H. Han and L. Sun, *ACS Catal.*, 2017, **7**, 1868–1874.

31 K. Dang, X. Chang, T. Wang and J. Gong, *Nanoscale*, 2017, **9**, 16133–16137.

32 S. Wang, L. Pan, J. J. Song, W. Mi, J. J. Zou, L. Wang and X. Zhang, *J. Am. Chem. Soc.*, 2105, **137**, 2975–2983.

33 Y.-C. Wang, Y.-Y. Zhang, J. Tang, H.-Y. Wu, M. Xu, Z. Peng, X.-G. Gong and G.-F. Zheng, *ACS Nano*, 2013, **7**, 9375–9383.

34 Y. Park, K. J. McDonald and K. S. Choi, *Chem. Soc. Rev.*, 2013, **42**, 2321–2337.